Optically enabled magnetic resonance study of ^{75}As and ^{121}Sb in ^{28}Si

Jeff Z. Salvail,[1] Phillip Dluhy,[1] Kevin J. Morse,[1] Michael Szech,[2] Kamyar Saeedi,[1] Julian Huber,[1] Helge Riemann,[3] Nikolai V. Abrosimov,[3] Peter Becker,[4] Hans-Joachim Pohl,[5] and Michael L. W. Thewalt[1,*]

[1]*Department of Physics, Simon Fraser University, Burnaby, British Columbia, Canada V5A 1S6*

[2]*Walter Schottky Institute, Technische Universität München, 85748 Garching, Germany*

[3]*Leibniz-Institut für Kristallzüchtung, 12489 Berlin, Germany*

[4]*PTB Braunschweig, 38116 Braunschweig, Germany*

[5]*VITCON Projectconsult GmbH, 07745 Jena, Germany*

(Received 5 August 2015; revised manuscript received 23 October 2015; published 30 November 2015; corrected 15 June 2016)

The electron and nuclear spins of donor impurities in enriched ^{28}Si have great potential as long-lived qubits for a silicon-based quantum information technology. The ability to resolve the hyperfine-split neutral donor ground-state levels in the near-infrared donor bound exciton transitions of the ubiquitous phosphorus impurity in highly isotopically enriched ^{28}Si has led to new methods of hyperpolarizing and measuring the donor electron and nuclear spins. This has resulted in optically assisted magnetic resonance methods that have permitted the measurement of remarkably long nuclear coherence times for both the neutral and ionized phosphorus donor in very lightly doped and highly enriched ^{28}Si. Other shallow donors such as arsenic, antimony, and bismuth offer the potential of larger hyperfine couplings and nuclear spins as compared to phosphorus. Here, we investigate whether donor bound exciton transitions can be used to initialize and read out the nuclear spins of arsenic and antimony in ^{28}Si. The projective readout of the electron and nuclear spins is demonstrated for both ^{75}As and ^{121}Sb, and these optical transitions can strongly hyperpolarize the nuclear spin of ^{75}As. Only a small nuclear hyperpolarization is achieved for ^{121}Sb, likely due to the relative weakness of the no-phonon transition of the Sb donor bound exciton. Optically assisted EPR and NMR is demonstrated for ^{75}As, including Hahn echo coherence time measurements of the six NMR transitions.

DOI: 10.1103/PhysRevB.92.195203 PACS number(s): 78.55.Ap, 78.20.Ls, 71.35.−y

I. INTRODUCTION

The electron and nuclear spins of neutral donors (D^0) in silicon are amongst the most promising and well-studied candidates for a semiconductor-based quantum information technology [1]. Silicon has the advantage of building upon the highly developed silicon device nanotechnology, and relatively standard metal-oxide-semiconductor technology has already been adapted to demonstrate the high-fidelity initialization, control, and readout of both the electron [2] and nuclear [3] spins of single phosphorus (^{31}P) donors using spin-dependent tunneling. This marks an essential step towards a scalable silicon-based quantum technology. Silicon also offers a relatively spin-free host environment, with only ∼4.68% of the atoms in natural silicon (hereinafter Si) having a nonzero nuclear spin, as compared to 100% of the host atoms in III-V semiconductors. This advantage can be greatly increased using isotopic enrichment to reduce the concentration of the ^{29}Si (nuclear spin $I = 1/2$) and increase that of ^{28}Si ($I = 0$), which already constitutes ∼92.23% of Si (the remainder is ^{30}Si, also with $I = 0$). Conventional electron paramagnetic resonance (EPR) [4], electron-nuclear double resonance (ENDOR) [5], and nuclear magnetic resonance (NMR) [6] have demonstrated dramatic improvements of the electron and nuclear coherence times of ensembles of ^{31}P in ^{28}Si. Nanodevices capable of studying single ^{31}P donors have now been fabricated using epitaxial layers of ^{28}Si, demonstrating electron coherence times of 0.5 s and nuclear coherence times >30 s [7].

Highly enriched ^{28}Si has another unique property which has nothing to do with the host nuclear spins, namely the elimination of inhomogeneous broadening caused by the mixed host isotopes. This results in a variety of optical transitions being far sharper in ^{28}Si than in Si [8,9]. The narrowing of the donor bound exciton (D^0X) transitions associated with ^{31}P in ^{28}Si allowed the hyperfine-split donor ground-state levels to be resolved, providing a projective readout of both the $S = 1/2$ electron spin and $I = 1/2$ nuclear spin [10]. These same D^0X transitions in ^{28}Si can be used to rapidly hyperpolarize the electron and nuclear spins of ^{31}P, as a result of the efficient Auger ionization of D^0X created resonantly from a specific D^0 hyperfine state [11]. This led to optically enabled magnetic resonance methods [12] that were capable of studying the residual ^{31}P present in the most highly enriched and chemically pure ^{28}Si available [13], resulting in nuclear coherence times of over 180 s for neutral ^{31}P [14] and 3 hours for ionized ^{31}P at cryogenic temperatures, and 39 minutes for ionized ^{31}P at room temperature [15]. The initialization and photoconductive readout of the electron spin state using D^0X transitions has been shown to be a useful adjunct to conventional EPR spectroscopy even for samples where the nuclear hyperfine states cannot be resolved [16]. The projective readout of D^0 electron and nuclear spins using Auger photoionization of resonantly created D^0X should be applicable to single-donor nanodevices where it could relax the requirements for very high magnetic field and very low temperature imposed by spin-dependent tunneling. However, there are problems related to the shifts and splittings of the D^0X transitions due to the local strains and electric fields inherent in such nanodevices [16].

*Corresponding author: thewalt@sfu.ca

TABLE I. Hyperfine parameters for shallow donors in Si.

Donor	I	g_e	g_n	A (MHz)
^{31}P	$\frac{1}{2}$	1.99850[a]	2.2632[b]	117.53[a]
			2.2607[d]	117.523936[d]
^{75}As	$\frac{3}{2}$	1.99837[a]	0.9596[b]	198.35[a]
			0.95[c]	198.32[c]
^{121}Sb	$\frac{5}{2}$	1.99858[a]	1.3454[b]	186.80[a]
^{123}Sb	$\frac{7}{2}$	1.99858[a]	0.7285[b]	101.52[a]
^{209}Bi	$\frac{9}{2}$	2.0003[a]	0.9134[b]	1475.4[a]
				1475.05[e]

[a]G. Feher, Phys. Rev. **114**, 1219 (1959).
[b]Reference [20].
[c]As determined from the fit in Sec. III D.
[d]Reference [12].
[e]Reference [22].

While ^{31}P is the most studied shallow donor in Si, partly as a result of its presence as a residual impurity in even the purest Si and ^{28}Si, the other shallow donors arsenic (^{75}As, $I = 3/2$), antimony (^{121}Sb, $I = 5/2$ and ^{123}Sb, $I = 7/2$), and bismuth (^{209}Bi, $I = 9/2$) may have advantages, including their larger hyperfine splittings and nuclear spins. These larger nuclear spins could be used as qudits coupled to the electron spin qubit, providing a larger Hilbert space and the possibility of implementing quantum error correction codes [17]. The D^{0}X transitions of ^{209}Bi have been shown to provide information on both the electron and nuclear spins in Si [18] and ^{28}Si [19], but as of yet they have not been used to produce a nuclear hyperpolarization. Here, we investigate whether the D^{0}X transitions of ^{75}As and ^{121}Sb in ^{28}Si also reveal the D^0 hyperfine splittings, and whether they can be used to hyperpolarize the donor nuclear spin.

II. THEORY

Considering only the contact hyperfine interaction between the donor electron and nuclear spin, the spin Hamiltonian for the D^0 ground state in an applied magnetic field $B_0\hat{z}$ can be written

$$\mathcal{H}_{D^0} = g_e\mu_B B_0 S_z - g_n\mu_N B_0 I_z + \alpha\vec{S}\cdot\vec{I}, \qquad (1)$$

where g_e is the electron g factor, g_n the nuclear g factor, μ_B the Bohr magneton, μ_N the nuclear magneton, and α the hyperfine constant, which in frequency units is $\alpha/h = A$. Values of these constants for the shallow D^0 in Si are given in Table I. Note that the g_n values given in Ref. [20] are for bare nuclei, and there can be small chemical shifts between these values and the actual values in Si, so some g_n directly determined in Si are also given in the table. Also, the D^0 hyperfine constant is not "constant" in the sense that it is for isolated atoms in vacuum, but has a significant dependence on the isotopic composition of the host Si [21]. Furthermore, it has been shown that in ^{28}Si the value of A for ^{31}P decreases by 3116 Hz in changing the sample environment from a temperature of ∼1.3 K and a hydrostatic pressure of ∼133 Pa to ∼4.2 K and ∼10^5 Pa [12]. Similar effects are expected for the other donors, but due to the small size of the effects they may only be observable in ^{28}Si.

The eigenvalues of Eq. (1) are given by the Breit-Rabi formula, as shown schematically for ^{121}Sb at the bottom left of Fig. 1. For $B_0 = 0$, there are two solutions, with total spin $F = I+1/2$ and $F = I-1/2$, separated by $A(I+1/2)$, with the lower F states lying lower in energy. For $B_0 > 0$, each of these states splits into $2F+1$ Zeeman components. One way of labeling the D^0 Zeeman states is from $|1\rangle$ to $|4(I+1/2)\rangle$ in order of increasing energy as shown in Fig. 1 (remembering that at very high B_0, beyond the range investigated here,

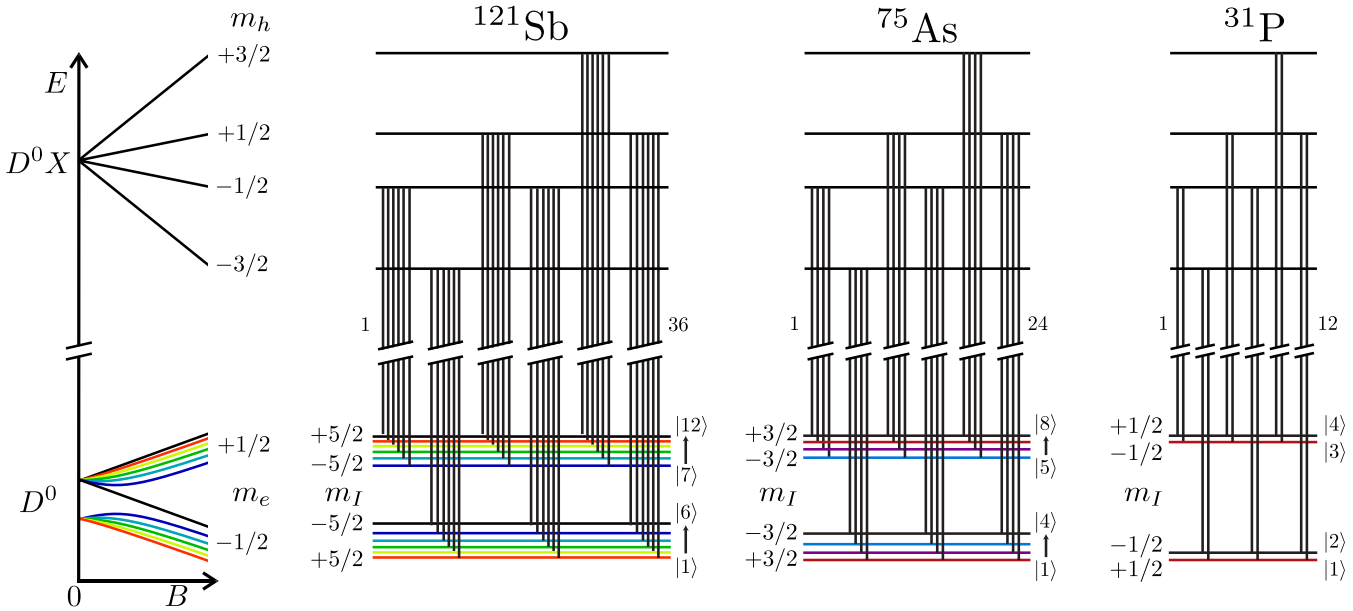

FIG. 1. (Color online) (Left) Energy levels of D^0 and D^{0}X for ^{121}Sb as a function of static magnetic field B_0. For D^0, the electron spin labels the "branch" as top or bottom (spin up or down, respectively), and the nuclear spin labels the hyperfine state on each branch. (Right) Optical transitions from D^0 to D^{0}X, in order of increasing energy, for the donors ^{121}Sb, ^{75}As, ^{31}P. D^0 states are labeled in order increasing energy. Note that the m_e and m_I labels are approximate, but approach pure states at high field, as described in the text.

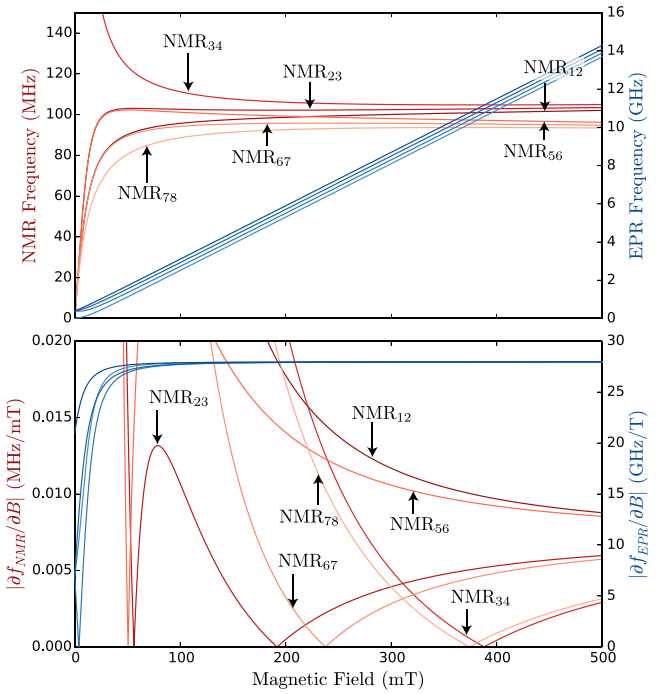

FIG. 2. (Color online) Calculated NMR and EPR transition frequencies and derivatives of the frequencies with respect to field for ^{75}As. (Top) Calculated NMR frequencies are shown in red (vertical scale on the left). EPR frequencies are shown in blue (vertical scale on the right). (Bottom) Derivatives of frequencies with respect to field $|\partial f_{\mathrm{NMR/EPR}}/\partial B_0|$. The cusps where these curves touch zero indicate clock transitions: the frequency is locally independent of field. Note again the different vertical scales on left and right.

there can be crossings of some levels). The states can also be labeled as if they were pure electron and nuclear spin product states, $|m_e,m_I\rangle$, although this is strictly true only for the $|1/2,+I\rangle$ and $|-1/2,-I\rangle$ states, all others being mixed by the hyperfine interaction. The product state description becomes asymptotically correct in the high-field limit as the mixing approaches zero, and is useful at intermediate and high fields for distinguishing between NMR-like transitions ($\Delta m_e = 0, \Delta m_I = \pm 1$) and EPR-like transitions ($\Delta m_e = \pm 1$, $\Delta m_I = 0$). The frequencies of these NMR-like and EPR-like transitions for ^{75}As and B_0 between 0 and 500 mT are shown at the top of Fig. 2, where NMR_{ij} labels an NMR-like transition between D^0 states $|i\rangle$ and $|j\rangle$, and similarly EPR_{lm} labels an EPR-like transition between states $|l\rangle$ and $|m\rangle$.

Of particular interest are points where the derivative of the transition frequency versus B_0 is zero, since at these so-called clock transition (CT) points the transition frequency is relatively insensitive to magnetic field noise, fluctuations and inhomogeneity, resulting in decreased transition linewidths, and increased coherence times of superposition states [12,22]. Derivatives of EPR and NMR frequencies versus B_0 are shown for ^{75}As in the bottom panel of Fig. 2, revealing a number of EPR and NMR CTs.

We now consider the $\mathrm{D}^0\mathrm{X}$ transitions, which are central to our method of preparing and measuring the D^0 spins. $\mathrm{D}^0\mathrm{X}$ can be created by capture of a free exciton (a Coulomb-bound electron hole pair that is free to move in the lattice and can be created by absorption of an above-gap photon) onto a D^0. The $\mathrm{D}^0\mathrm{X}$ Zeeman states are rather simple, since the two electrons form a spin singlet which does not couple to B_0, the 3/2 hole spin, or the donor nuclear spin. The p-like hole states have negligible contact hyperfine interaction with the donor spin, and the bare donor nuclear Zeeman term in the $\mathrm{D}^0\mathrm{X}$ energy can be ignored, since it is much smaller than the optical linewidths. $\mathrm{D}^0\mathrm{X}$ can also be created resonantly by the absorption of a photon whose energy matches the energy difference between a populated D^0 state and a $\mathrm{D}^0\mathrm{X}$ state. Since these are no-phonon transitions, the $\mathrm{D}^0\mathrm{X}$ can decay to the original D^0 state by emitting a luminescence photon at the same energy as the initial photon. The strength of the $\mathrm{D}^0\mathrm{X}$ absorption transitions are proportional to the D^0 hyperfine populations, while the emission transitions are not, so it is the absorption transitions which are used to measure these populations.

Due to its indirect band gap, $\mathrm{D}^0\mathrm{X}$ absorption in Si is extremely weak, so the absorption signal is best detected indirectly, for example, by detecting the luminescence of the created $\mathrm{D}^0\mathrm{X}$, using photoluminescence excitation spectroscopy (PLE) [12]. However, the $\mathrm{D}^0\mathrm{X}$ photoluminescence signal is also relatively weak, with a quantum efficiency of less than 10^{-4}, due to the very short nonradiative Auger decay times [23,24] compared to the radiative decay time, which is much longer due to the indirect band gap. In the Auger process, one of the $\mathrm{D}^0\mathrm{X}$ electrons recombines with the hole, and the other is ejected with $\sim$1 eV of kinetic energy. The photoconductive signal due to these Auger electrons provide another means of indirectly determining the $\mathrm{D}^0\mathrm{X}$ absorption strength [14,15], and Auger recombination is also essential for the resonant optical hyperpolarization process [25]. Resonant Auger photoionization of D^0 is also central to attempts to combine optical $\mathrm{D}^0\mathrm{X}$ methods with single donor nanodevices.

III. EXPERIMENT & RESULTS

A. Sample

The sample studied for this research was a 5 × 4 mm section of a 2-mm thick slice of a ^{28}Si crystal that contains phosphorus, arsenic, and antimony impurities. This crystal was grown from existing Avogadro material [13] enriched to 99.995% ^{28}Si, and was doped with 99.6% enriched ^{121}Sb. The ^{75}As and ^{31}P found in the sample must have been present in the ^{121}Sb source material. After being cut to size, the sample was etched in 10 : 1 mixture of HNO_3 : HF, which removes any surface damage accumulated during the cutting. The sample is n-type with dopant concentrations determined by photoluminescence spectroscopy shown in Table II.

TABLE II. Sample dopant concentrations.

Dopant	Concentration (cm^{-3})
^{31}P	4×10^{14}
^{75}As	5×10^{14}
^{121}Sb	1×10^{14}
B	7×10^{13}

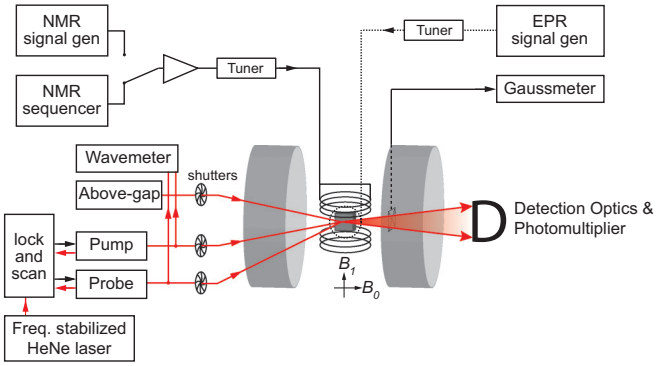

FIG. 3. (Color online) Schematic of the experimental setup. See text for discussion.

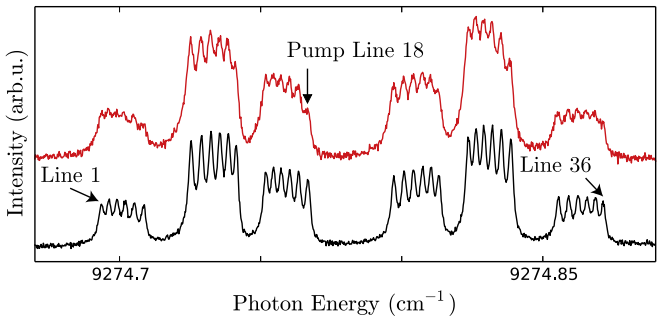

FIG. 4. (Color online) Antimony PLE spectra. Conditions common to both spectra: $B_0 = 110$ mT; probe power 100 mW; pump power 400 mW; above-gap excitation 12 mW. (Bottom trace) Simple PLE spectrum, no pump, only probe. [Top trace (red)] PLE spectrum with pump laser tuned to line 18, which excites hyperfine state $|7\rangle$.

B. Experiment

The experimental setup, shown in Fig. 3, is similar to that used in previous work on phosphorus donors [14,15]. The measurement process is essentially the same: tunable single-frequency lasers are brought into resonance with a D^0X transition and the decay of the exciton is detected. Since D^0X have a small binding energy, these experiments must be performed at or below 4.2 K. In this case, ∼1.4 K was used in order to eliminate the bubbles present in helium above the lambda point. An electromagnet provides the static field B_0.

There are three lasers used. The first, called the probe, is a Koheras Adjustik fibre laser. This is locked to an external cavity, which is itself locked to a frequency stabilized helium neon standard. The probe is amplified by an IPG Photonics ytterbium fibre amplifier. The second laser, called the pump, is a Toptica Photonics DL100 Pro diode laser, amplified by a Keopsys fibre amplifier. This laser is locked to the same cavity.

In the laser beam lines are shutters (SRS SR475) and a chopper wheel, the latter to allow lock-in detection. The pump and probe are also fed into a wavemeter (Bristol 621) so their energies can be mutually calibrated. The probe is used as the sweeping laser to collect D^0X optical spectra. The probe is also used in fixed-frequency mode together with the pump for the magnetic resonance experiments. The pump and probe are used to excite selected D^0X transitions (per experiment, they can each be tuned to any one).

The third laser is a Nd:YLF laser (CrystaLaser) at 1047 nm; it is called the above-gap laser since its photons have energy exceeding the silicon band gap. The above-gap light creates free carriers within the sample, which in turn helps to neutralize donors and acceptors that have been ionized. This reduces random electric fields that can produce Stark broadenings of the optical transitions, resulting in sharper D^0X lines.

There are several RF sources used: an NMR sequencer (Spincore PulseBlaster DDS) for pulsed NMR experiments, an Agilent M8190A arbitrary waveform generator for continuous wave (CW) NMR experiments with fixed frequencies, and an SRS SG384 signal generator for CW NMR or EPR frequency sweeps.

The sample was held in a strain free manner, centered in the high magnetic field region of two resonant circuits for coupling the RF signals to the spins in the sample. The NMR coil is a Helmholtz pair with a total of six turns. It is oriented to create an oscillating magnetic field B_1 perpendicular to B_0 and is tuned to the relevant spectral region near 100 MHz. The EPR coil consists of a single turn loop-gap resonator tuned to ∼2850 MHz that is oriented to create a magnetic field perpendicular B_0 and B_1. Since the coils are used only for coupling radiation into the sample and not for NMR/EPR detection, these resonators have low Q factors and do not need to be particularly well matched to the 50-ohm transmission lines. Moreover, since we operate at a fixed field and need to access several transitions, a broader resonance is advantageous, allowing simultaneous coupling to multiple transitions.

We used both PLE detection and Auger photoconductivity detection to monitor the D^0X absorption. In this sample, PLE detection gave a better SNR, likely due to the relatively high donor concentration, and was used for all the following measurements. Spatial and spectral filters gather the photoluminescence and isolate the signal from the laser illumination. Because the laser illumination excites the D^0X no-phonon line, the high-rejection spectral filter is tuned to the D^0X single-phonon transverse optical phonon replica so that the scattered excitation light does not overwhelm the detector. The filtered signal is then detected by a Hamamatsu H10330A-25 photomultiplier.

C. PLE Spectroscopy

We begin characterizing the ^{121}Sb and ^{75}As dopants by examining the D^0X transitions with photoluminescence excitation (PLE) optical spectroscopy. The sample is illuminated with the chopped probe laser and the resulting photoluminescent response is detected using a lock-in amplifier and recorded as a function of probe frequency. The response may also be modified by the presence of other laser illumination or RF irradiation.

First we study ^{121}Sb. Of the group-V donors in the sample, ^{121}Sb has the highest nuclear spin, and hence is of great interest. Under suitable conditions (high enough magnetic field, some above-gap excitation) the 36 $D^0 \rightarrow D^0X$ transitions are well-resolved, as seen in the bottom trace of Fig. 4. This level of resolution is possible due to the high isotopic enrichment and chemical purity of the sample; in natural silicon the individual

nuclear spin states cannot be resolved [8,9]. Thus the readout of individual ^{121}Sb D^0 hyperfine state populations using the D^0X transitions is confirmed to be effective.

The next experiment is to attempt polarization of ^{121}Sb D^0 into a single hyperfine state. The pump laser, more intense than the probe used for readout, is tuned to D^0X line 18. Based on the earlier results for ^{31}P, this should produce an optimal hyperpolarization, since it pumps D^0 in the $|+1/2,-5/2\rangle$ state to D^0X, where an electron spin flip (brought about by Auger ionization of the D^0X and recapture of a spin-down electron) results in the $|-1/2,-5/2\rangle$ state, which is a pure state without any hyperfine mixing [25]. Another D^0X spectrum is then gathered in the presence of this optical pumping by sweeping the probe laser across all transitions. As seen by comparing the top and bottom traces of Fig. 4, the pump laser produces a small decrease in the $|+1/2,-5/2\rangle$ population, and almost zero net electron polarization.

We believe that the very weak hyperpolarization obtained by pumping the D^0X transitions of ^{121}Sb results from the relatively weak no-phonon transition of the Sb D^0X as compared to the P, As, and Bi D^0X. The relative no-phonon strengths for the different donors depend very strongly on the donor central cell potentials. The resonant D^0X hyperpolarization process is in all cases in competition with the nonresonant ionization of the D^0, independent of their hyperfine state, resulting from the high energy tails of their photoionization continua. For ^{121}Sb, the resonant D^0X absorption must be weaker than the nonresonant photoionization process, while for P and As (and presumably Bi), the resonant process must dominate, at least in highly enriched ^{28}Si.

While the direct hyperpolarization of ^{121}Sb using its D^0X transitions was unsuccessful, we were able to observe a significant Sb nuclear hyperpolarization using a cross-polarization effect. Here, we resonantly create phosphorus D^0X by pumping phosphorus $D^0 \rightarrow D^0X$ transitions with the pump laser, while using the probe to gather a PLE spectrum of antimony. In order to maximize the effect, no above-gap excitation was used, and due to the resulting Stark broadening, the individual phosphorus lines were not resolved, so the laser pumped instead a doublet with common electron spin. The results are shown in Fig. 5. Here, we can see clear evidence for nuclear hyperpolarization, the direction of which depends on the phosphorus D^0 state being pumped. In particular, pumping a spin-down (up) phosphorus electron state leads to a positive (negative) antimony nuclear spin polarization, indicating that the ^{121}Sb nuclear hyperpolarization is due to cross relaxation between ^{31}P donor electrons interacting with nearby ^{121}Sb electrons, inducing an electron spin polarization on the ^{121}Sb, evidence for which can be seen in Fig. 5. The polarization of the ^{121}Sb electrons could come about directly via ^{31}P to ^{121}Sb coupling, or indirectly via the partially polarized free electrons produced by Auger recombination of the ^{31}P D^0X. This in turn produces a polarization of the antimony nuclear spins via the Overhauser effect.

Since the ^{121}Sb D^0 hyperfine system was not able to be effectively hyperpolarized, we were unable to study its NMR/EPR behavior and measure its nuclear spin coherence times. While our investigation on antimony ends here, other techniques could be used for nuclear polarization (such as an appropriately modified version of the protocol used in Ref. [26] to polarize ^{31}P), while the effective readout using D^0X transitions can still be employed.

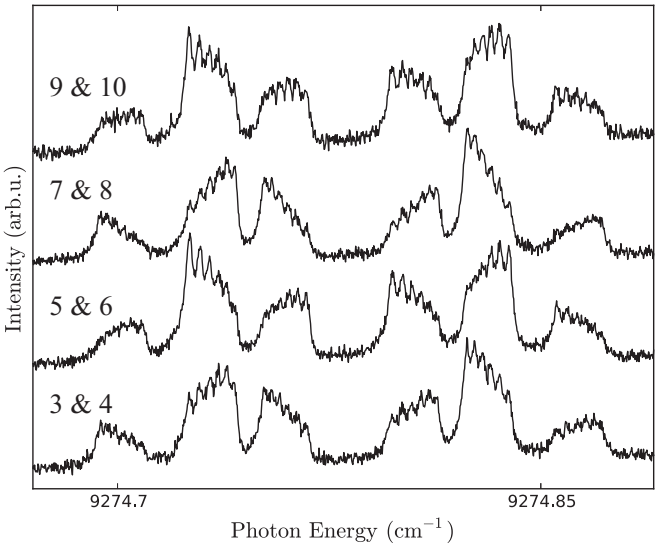

FIG. 5. Cross-polarization of antimony by resonant creation of phosphorus bound excitons. Conditions common to all spectra: $B_0 =$ 110 mT; probe power 126 mW; pump power 250 mW; above-gap excitation: none. From bottom to top: antimony PLE spectrum collected while the probe laser is tuned to phosphorus D^0X lines 3 and 4, 5 and 6, 7 and 8, and 9 and 10 (as labeled in Fig. 1).

We now turn our attention to the donor ^{75}As. As in the previous experiment, we begin by collecting an unpumped PLE spectrum by sweeping the probe laser across the 24 $D^0 \rightarrow D^0X$ transitions. The result is the middle trace of Fig. 6. As with ^{121}Sb, we can resolve all $D^0 \rightarrow D^0X$ transitions (24 for ^{75}As), demonstrating that the individual hyperfine states

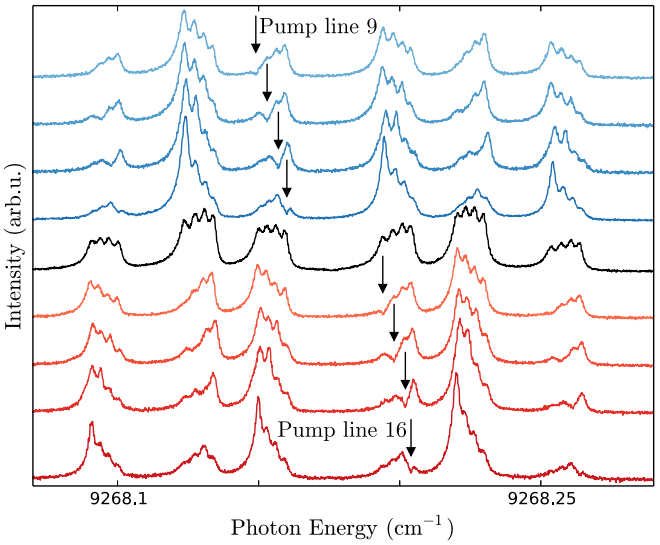

FIG. 6. (Color online) Arsenic PLE spectra. Conditions common to all spectra: $B_0 = 110$ mT; probe power 100 mW; pump power 400 mW; above-gap excitation: none. [Middle trace (black)] Single-laser unpumped PLE spectrum. (Coloured traces) From top to bottom, the pump laser is tuned to lines 9 through 16 as indicated by the arrows. This corresponds to pumping D^0 states $|8\rangle$ through $|1\rangle$.

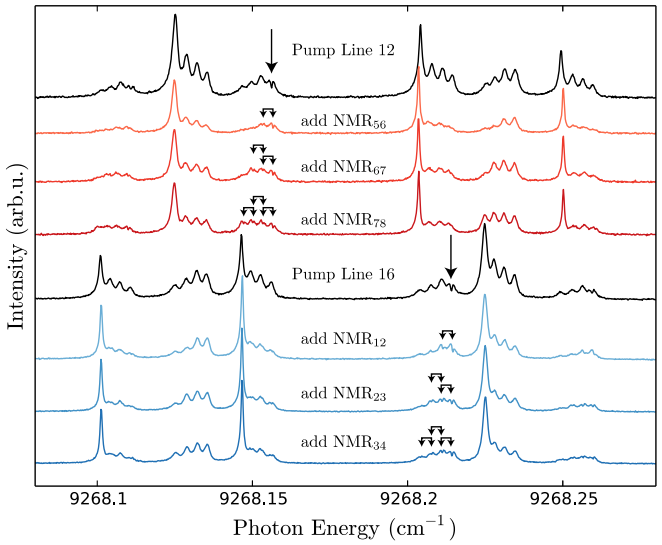

FIG. 7. (Color online) Arsenic PLE spectra with RF. Conditions common to all spectra: $B_0 = 110$ mT; probe power 200 mW; pump power 400 mW; above-gap excitation: 12 mW; RF output power 33 dBm (actual power delivered to coil varies with frequency due to coil matching). (Trace 1) Pump tuned to line 12, pumping state $|5\rangle$. [Traces 2–4 (red)] In addition to the optical pump on state $|5\rangle$, these traces show the effect of consecutively turning on NMR_{56}, NMR_{67}, NMR_{78}. [Trace 5 (black)] Pump tuned to state $|1\rangle$. [Traces 6–8 (blue)] In addition to the optical pump on state $|1\rangle$, these traces show the effect of consecutively turning on NMR_{12}, NMR_{23}, NMR_{34}.

can be optically addressed. Next, we add the pump laser, and tune it to each of the hyperfine states $|1\rangle$ through $|8\rangle$, gathering a spectrum for each. As evident in Fig. 6, the pump laser has a significant effect on the spectrum and burns spectral holes at the energy of the pump laser in each spectrum, a feature that indicates significant population depletion of the state. Moreover, each spectral hole is accompanied by an enhancement in the population of the state with the same nuclear, but opposite electron spin. The effect is most pronounced when pumping lines 12 and 16, which correspond to pumping states $|5\rangle$ and $|1\rangle$, respectively. These two states are the mixed states with electron spin opposite that of the two pure spin states ($|4\rangle$ and $|8\rangle$, respectively), confirming that, just as with ^{31}P, pumping into a pure state is the most effective way to hyperpolarize the system.

Now, we attempt to enhance the polarization further by using CW NMR excitation to saturate the populations of adjacent nuclear spin states, hopefully bringing more population into resonance with the laser. These experiments consist of tuning the pump laser to a $D^0 \rightarrow D^0X$ transition, applying one or several NMR B_1 fields, and scanning the probe laser across the 24 optical transitions. Results of these experiments are seen in Fig. 7.

The first set of experiments consist of pumping line 12, corresponding to state $|5\rangle$, which, as demonstrated above, was the most effective way to polarize the system into an electron spin down hyperfine state $|4\rangle$. Then in turn, each of the three NMR transitions are activated. First, NMR_{56} mixes the population of $|6\rangle$ with $|5\rangle$, the state being pumped by the laser. Next, NMR_{67} and NMR_{56} are used to mix the populations of $|5\rangle$, $|6\rangle$, and $|7\rangle$. Finally, NMR_{78}, NMR_{67}, and NMR_{56} are used to mix states $|5\rangle$ through $|8\rangle$, all the states in the electron spin-up branch. We observe that turning on NMR_{78} and NMR_{67} seems to reduce the achievable polarization, rather than increasing it. This must reflect the competition between bringing populations from $|8\rangle$ and $|7\rangle$ towards $|6\rangle$ and then $|5\rangle$ for ionization, versus the removal of population from $|6\rangle$ towards $|7\rangle$ and $|8\rangle$, which could likely be better optimized by adjusting the relative rates. The same trend is observed when pumping line 16 (pumping out of $|1\rangle$ into $|8\rangle$) and in turn activating NMR_{12}, NMR_{23}, and NMR_{34}. From this, we conclude that the most effective way to hyperpolarize the ^{75}As system under our conditions uses a pump laser set to promote D^0 in either $|5\rangle$ or $|1\rangle$, depending on the desired electron spin, and a single NMR transition, corresponding to the transition between the laser-pumped state and the adjacent nuclear state having the same m_e.

By fitting the spectra for all 24 lines we can determine the population changes and associated polarization of each spectra in Fig. 7. When pumping $|5\rangle$ and applying NMR_{56}, we achieve a maximum electron polarization of -0.32. In this configuration 40% of the arsenic donors are in state $|4\rangle$, which is a factor of 3.2 increase over the equilibrium population. When pumping $|1\rangle$ and applying NMR_{12} we achieve a maximum electron polarization of $+0.26$. In this configuration, 36% of the arsenic donors are in a state of $|8\rangle$ which is a factor of 2.9 increase over the equilibrium population. The electron and nuclear polarizations achieved here are significantly less than observed previously for ^{31}P [14]. This likely resulted from the much higher D^0 concentration used here, and the greater inhomogeneous linewidths of the D^0X transitions.

D. Optically detected NMR and EPR scans

In this section, we show the results of optically detected CW NMR and EPR spectroscopy. The sample is illuminated with both the pump and probe lasers at fixed frequencies, the NMR or EPR frequency is scanned, and the photoluminescent response is recorded as a function of this frequency. The probe beam is chopped and the signal detected using a lock-in amplifier.

We refer now to Fig. 8 where the six NMR transitions between the eight hyperfine states appear as dips or peaks on the background. A fit to the spectrum using the Breit-Rabi formula to place a Lorentzian at each transition frequency is shown. Parameters for the fit included a linear background subtraction, hyperfine constant A, magnetic field B_0 (which is assumed to differ slightly between location of the gaussmeter and the sample), and the nuclear g-factor g_n. A Lorentzian lineshape, with height and width as free parameters, is used because under these conditions the primary contributor to the linewidth is power broadening. This is confirmed by measuring NMR_{56} at a variety of powers, revealing a lowest width of 12 kHz at -17 dBm applied to the resonator (compare with the width of 340 kHz in Fig. 8, done at 7 dBm applied power). The best fit parameters were $A = 198.32 \pm 0.06$ MHz and $g_n = 0.95 \pm 0.04$.

Because high RF power was required to detect all six NMR transitions in a single scan and the coil resonance is narrower than the scan region, the measured heights and widths are

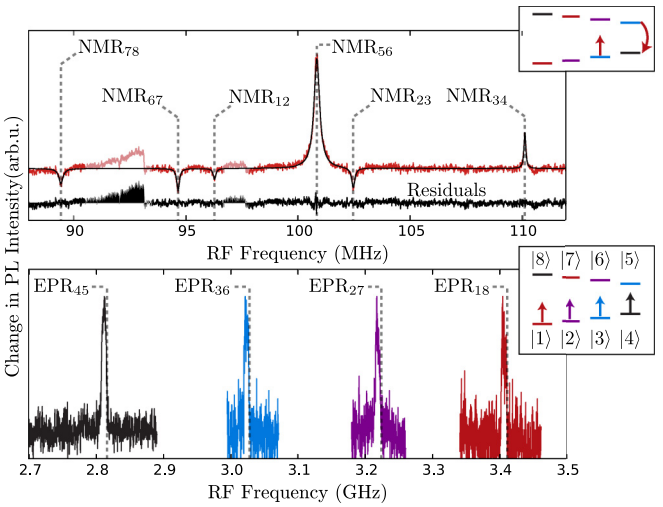

FIG. 8. (Color online) (Top) Arsenic optically detected NMR spectrum, taken at $B_0 = 110$ mT, pump tuned to line 12 (emptying state $|5\rangle$), probe tuned to line 14 (reading state $|3\rangle$), see inset. Pump power 400 mW, probe power 300 mW (note that the probe is chopped so the average power is a factor ∼2 smaller). No above-gap excitation was used. A fit to the spectrum, using the Breit-Rabi formula to place a Lorentzian (whose height and width are fit parameters) at each transition frequency, is shown in black. Residuals shown below. (Bottom) Arsenic EPR spectra (scaled to same height), taken at $B_0 = 110$ mT. From left to right, 300 mW probe tuned to lines 13 through 16 (states $|4\rangle$ through $|1\rangle$). No above-gap excitation was used. Dotted lines indicate the expected location of EPR transitions based on the parameters determined by the NMR fit.

strongly dependent on the coil matching. Positive amplitudes are observed when applying NMR_{56} and NMR_{34} since these transitions increase the population available to empty into $|4\rangle$ (NMR_{56}) and pump into $|6\rangle$ (NMR_{34}). That the other transitions have negative amplitude implies the removal of population from states directly involved in the pump/probe scheme is stronger than the movement of population towards them. This relates to the results shown in Fig. 7 where applying RF to more than one transition reduces the observable polarization. The semitransparent features from ∼91–93 and ∼97 MHz were excluded from the fit. We attribute these features to heating of the system by the RF NMR signal, as they coincide with a rise in the measured vapour pressure of the helium bath and occur at frequencies nearest to where the coil is impedance matched.

By scanning microwave frequency excitation in a way similar to the previously mentioned NMR scans, we can generate optically detected EPR scans of the ^{75}As donors. The results are shown in the bottom panel of Fig. 8. These EPR spectra have very poor signal-to-noise and a very broad lineshape. We attribute the poor lineshape to B_0 inhomogeneity due to our small and unoptimized electromagnet. These transitions are strongly affected by B_0 inhomogeneity while the NMR lineshapes remain quite Lorentzian despite both being taken in the same B_0 field. Referring back to Fig. 2, we see that at 110 mT the frequencies of the EPR transitions are several orders of magnitude more sensitive to fluctuations and inhomogeneity in B_0 than those of the NMR transitions.

The poor signal-to-noise results largely from the spreading of the EPR spectra due to the inhomogeneity in B_0. Also, the EPR coil was tuned to the first EPR transition, $EPR_{45} \approx 2800$ MHz, and at higher EPR frequencies the signal when using fixed microwave drive power is reduced. The EPR frequencies are predicted based on the fit to the NMR spectrum and are indicated in the bottom panel of Fig. 8. The small systematic shift between the observed and predicted transition frequencies is likely due to inexact knowledge of B_0 at the sample location. With improvements in the homogeneity of the B_0 field and concomitant reductions in the EPR linewidths, the EPR transition frequencies, combined with the known value of g_e, could be used to provide more accurate values for B_0.

E. Pulsed NMR

Finally, in this section we show the results of pulsed NMR experiments. The protocol we established to prepare a pure initial state, perform the pulsed NMR operations, and read out the resultant state populations is seen in Fig. 9.

To access the electron spin-down branch, we polarize the system into state $|4\rangle$ by pumping D^0X line 12. By applying NMR_{56}, we mix $|5\rangle$ and $|6\rangle$, depleting the populations of both. The above-gap laser excitation narrows the transitions as discussed above. It was found by varying the duration of this step and studying the PLE of $|4\rangle$ that 100 ms is sufficient time to achieve maximum polarization. In order to polarize into $|8\rangle$ to access the electron spin-up branch, the same sequence is used except we pump line 16 and drive NMR_{12} to deplete both $|1\rangle$ and $|2\rangle$.

To read out the state of the nuclear spin, we employ quantum nondemolition measurement. To read out from the electron spin-down branch, resonant lasers tuned to lines 12 and 13 (states $|5\rangle$ and $|4\rangle$, respectively) pump both electron spin states for the given nuclear spin state ($-3/2$, in this case). Since each experiment is limited to a given electron spin branch, the signal from reading out state $|5\rangle$ can be considered part of the background signal. Readout for the electron spin-up branch is likewise done by simultaneously pumping lines 9 and 16 ($|8\rangle$ and $|1\rangle$, respectively, nuclear spin $+3/2$). During readout we also illuminate with above-gap excitation.

Due to the projective readout, all pulsed NMR experiments were collected one point at a time, with each point taking approximately one second plus the length of the pulse/wait time. The Rabi and Ramsey experiments took approximately five minutes each as they were comprised of 200 to 300 points with no averaging, while the Hahn echo results were the average of 3 to 5 scans taking approximately ten minutes each.

With initialization and readout in hand, we first perform a Rabi experiment on each qubit subspace to determine the π-pulse length of that particular NMR transition. Polarization and readout are limited to either state $|4\rangle$ or $|8\rangle$, depending on electron spin, adding complexity to the pulse sequences. For example, to initialize into $|2\rangle$, we require knowledge of π_{34} and π_{23} (meaning the π-pulse lengths for the subspaces spanned by $|3\rangle$ and $|4\rangle$, and $|2\rangle$ and $|3\rangle$) in order to shuttle population to $|2\rangle$. Readout requires applying these pulses in the opposite order to bring the desired population back to $|4\rangle$ where it can

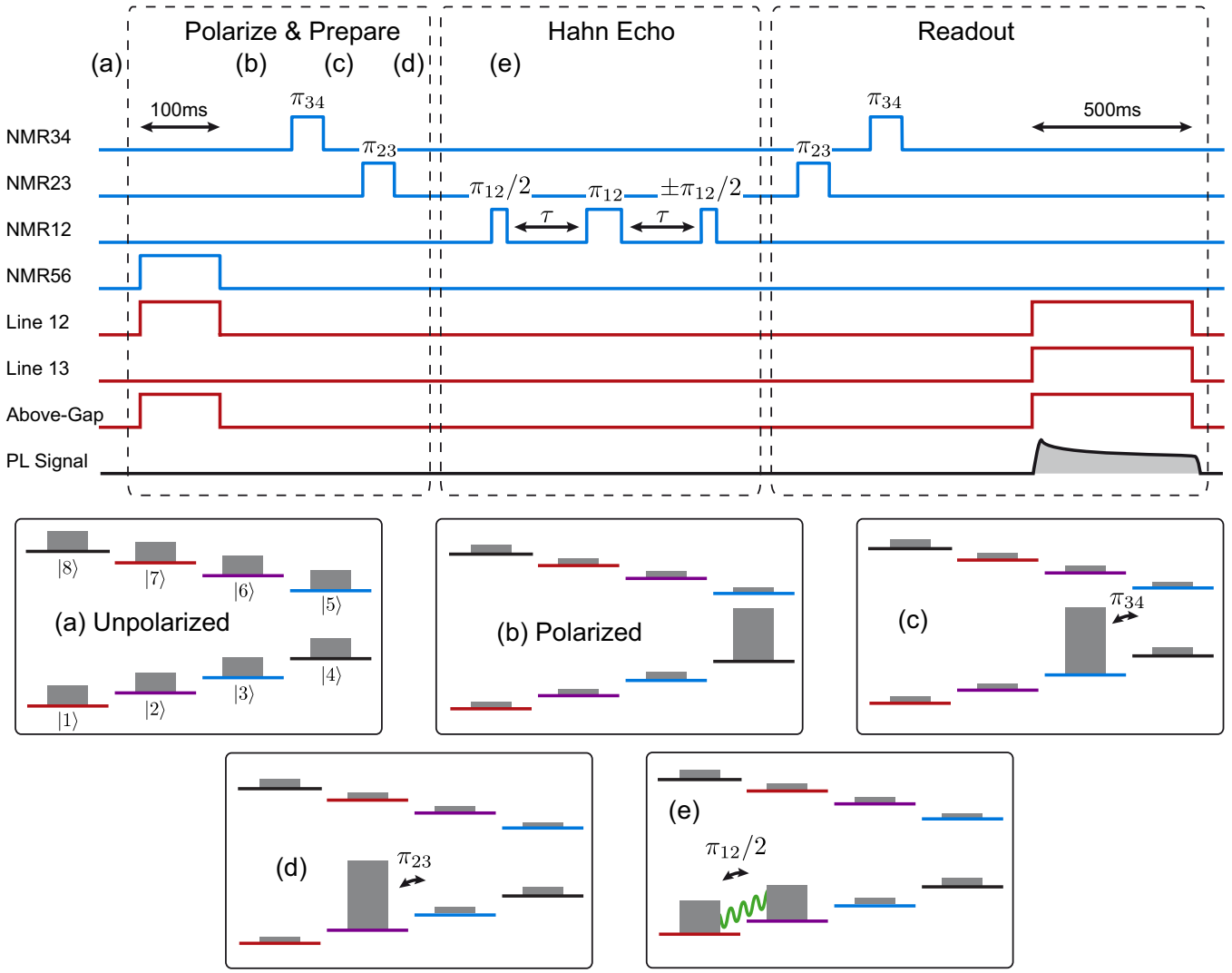

FIG. 9. (Color online) The complete experiment for a Hahn Echo measurement on the qubit subspace spanned by $|1\rangle$ and $|2\rangle$. The labels (a) through (e) indicate stages in the experiment leading up to the creation of quantum coherence after e). (a) We begin with an almost completely unpolarized hyperfine state. (b) Optical line 12 (state $|5\rangle$) is pumped while simultaneously applying NMR_{56} and above-gap illumination to initialize the system into $|4\rangle$. (c) An NMR_{34} π pulse moves the population to $|3\rangle$. (d) An NMR_{23} π pulse moves the population to $|2\rangle$. (e) An NMR_{12} $\pi/2$ pulse creates the superposition state $|+\rangle = (|1\rangle + |2\rangle)/\sqrt{2}$. For the Hahn echo, this state is allowed to evolve freely for time τ, after which an NMR_{12} π pulse refocuses the spins. Another time τ later, a second $\pi/2$ pulse projects the remaining coherence back to the z axis. For readout, the series of pulses is reversed, bringing the population back to $|4\rangle$ where it can be accessed by the readout lasers. The sequence can be appropriately modified to probe the spin-up electron branch, by using the lasers on lines 9 and 16, which polarizes into state $|8\rangle$.

be read out as a PLE signal induced by the lasers (see Fig. 9 for this sequence).

An example of Rabi oscillations is shown in Fig. 10. Note that the power applied for each Rabi pulse was tuned to achieve a pulse duration between 50 and 100 μs. This decreases the pulse bandwidths to reduce the chance of exciting other transitions.

Next, we perform Ramsey experiments, again using the same initialization and readout procedure. These experiments consist of two $\pi/2$ pulses separated by free evolution time τ. This allows us to probe both the dephasing time T_2^* and precisely measure the frequency of the transition. The results of some Ramsey experiments are shown in Fig. 11. It is interesting to note that the measurement taken with above-gap irradiation during the initialization and read out phase shows a slightly longer $T_2^* = 7.6$ ms as opposed to $T_2^* = 6.2$ ms.

The ultimate goal of the pulsed NMR experiments is to measure the nuclear spin coherence times. As discussed in connection with Fig. 2 and shown in Ref. [14], operating at a clock transition can extend the measured coherence time by reducing the effect of B_0 field inhomogeneities and fluctuations. The best way to find the clock transition is to accurately measure the NMR transition frequency as a function of field near the predicted clock transition, fit the result to the model, and extract the field of the clock-transition from the fit. These frequencies were measured using a Ramsey experiment and the result is shown in Fig. 12. The free parameters used in the fit are hyperfine constant A and arsenic nuclear g factor g_n,

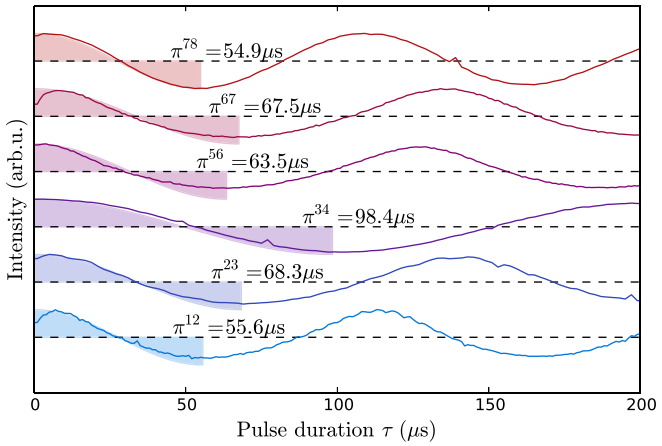

FIG. 10. (Color online) NMR transition Rabi oscillations. Each transition's Rabi oscillation is shown along with the π-pulse length, illustrated by the coloured region.

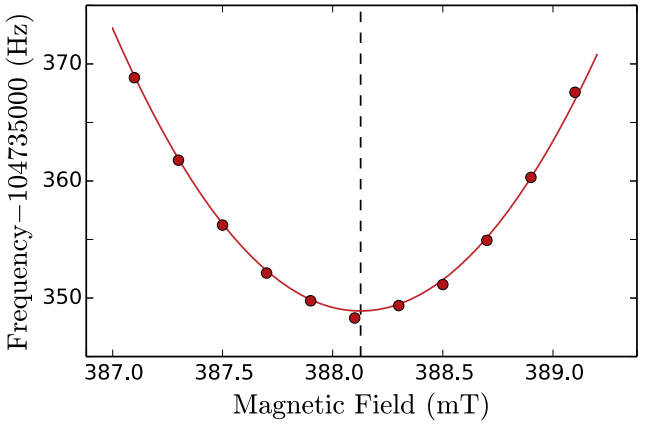

FIG. 12. (Color online) NMR_{34} frequency vs applied B_0. Data are points; the curve shows the best fit from the Breit-Rabi formula. The vertical dashed line shows the location of CT_{34} at $B_0 =$ 388.12 mT.

placing the clock transition at a field of 388.12 mT. This field will be referred to as CT_{34}. All subsequent pulsed experiments are performed at this field to reduce the linewidth and increase the coherence time of this transition.

Next, we move on to measuring the coherence time with the Hahn echo pulse sequence. A coherence is created between two adjacent nuclear spin states using a $\pi/2$ pulse as in the Ramsey experiment, but the presence of a refocusing π-pulse mitigates static (or slowly-varying) sources of dephasing, allowing the lifetime of the coherence to be measured. See Fig. 13 for Hahn echo decays measured for each NMR transition.

The decays were best fit using a stretched exponential,

$$e^{-(t/T_m)^{\beta}}, \tag{2}$$

where T_m is the time constant and β is stretch coefficient. Given the SNR, a single β of 1.39 was found to adequately fit all of the decays. $\beta > 1$ is suggestive of spectral diffusion [27], which refers to the time-dependent diffusion of spin angular momentum caused by the noise spectrum of the spin bath. The sample used in this experiment has donor concentrations orders of magnitude larger than that used in the previous work on ^{31}P [14], allowing for the possibility of spectral diffusion due to donor-donor dipolar interactions as the source of decoherence.

We were surprised, however, that the decay for NMR_{34} was not significantly longer than the other decays, given that we were operating at CT_{34}. This could suggest the existence of an additional decoherence mechanism. Given the relatively high donor concentration, donor-donor electron flip-flops likely make a significant contribution.

It is also worth noting that for NMR_{12} and NMR_{56}, the subspaces furthest from the initial polarization states $|4\rangle$ and $|8\rangle$, respectively, these particular measurements required averaging until an acceptable level of signal-to-noise was

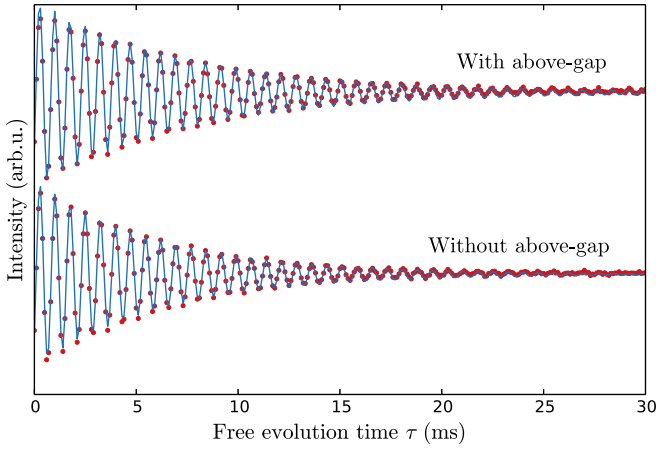

FIG. 11. (Color online) Ramsey fringes for transition NMR_{34} at static field $B_0 = 388.21$ mT, ω_{RF} detuned by ~1.3 kHz from the transition frequency. The Ramsey experiment is performed both with and without above-gap illumination during initialization and read out. Data shown in red circles, fit shown with blue line. T_2^* is slightly longer with than without above-gap excitation: 7.6 ms compared to 6.2 ms without.

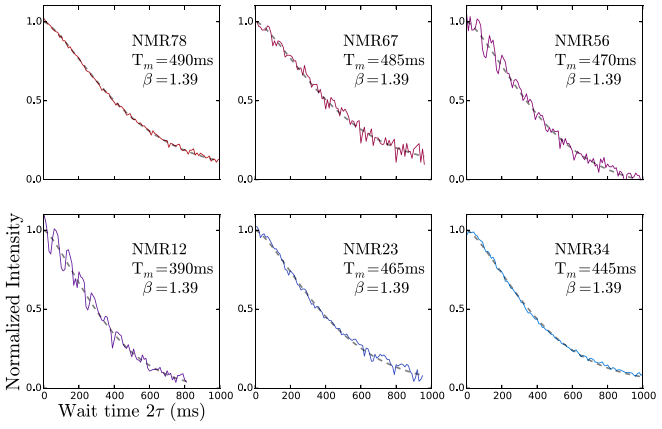

FIG. 13. (Color online) Hahn echo decays for each NMR transition, taken at $B_0 = 388.12$ mT (CT_{34}). All six plots are shown with the same horizontal and vertical scales and ranges. All decays normalized to unity at $\tau = 0$. The dashed lines are a stretched exponential fit to the data using the value of β, the stretch coefficient, that best fit the data. The time constant of each decay is indicated near the respective fit. See text for discussion.

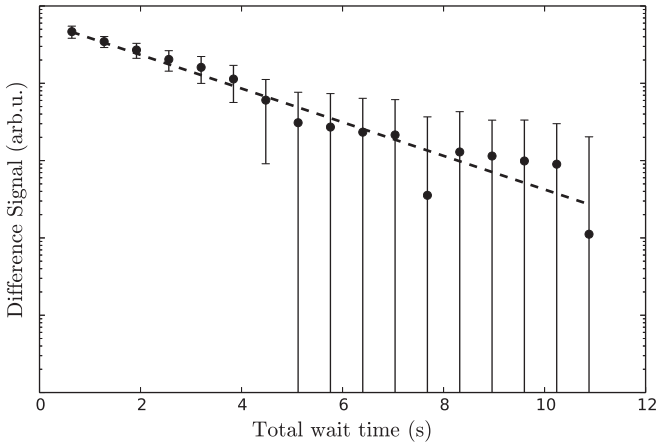

FIG. 14. XY16 decay for transition NMR_{34}, taken at $B_0 = 388.12$ mT (CT_{34}), with the time delay between sequential π pulses $\tau = 5$ ms. The data points are the average of 16 experiments; error bars represent the standard deviation of the data. Note the logarithmic scale distorts the error bars so they do not appear symmetric. The dashed line is a single exponential fit, giving the XY16 $T_2 = 2.0$ s.

reached. The decrease in signal-to-noise we observe as we move away from the initialization states is indicative of poor pulse fidelity. A significant amount of the signal is lost as we shuffle the population through the four dimensional nuclear spin Hilbert space.

Finally, we proceed to a measurement of the coherence time using the XY16 dynamic decoupling pulse sequence [14,15]. The measured XY16 coherence time seen in Fig. 14 for ^{75}As transition NMR_{34} is 2.0 s in this sample. The experiment was performed only between states $|3\rangle$ and $|4\rangle$ because there exists a clock transition between these two states at this field leading to, presumably, the most extensible coherence time. Although the sample used in this study is grown from the same source of isotopically enriched silicon as in Ref. [14], the XY16 coherence time is only two seconds as opposed to 180 s previously reported for ^{31}P. This shorter coherence is primarily due to the donor concentration. The 180 s result comes from a p-type sample with [P] $\approx 10^{11}$ cm^{-3}, while the current n-type sample has been doped such that [P] + [As] + [Sb] $\approx 10^{15}$ cm^{-3}. The considerably higher donor concentration allows significant donor-donor dipolar coupling that not only generates magnetic field noise but can also reduce T_2 via direct donor-donor flip flops [22]. That the XY16 dynamical decoupling only led to a small improvement in T_2 could again show that spectral diffusion is not the only source of decoherence.

In conclusion, optically creating D^0X in ^{28}Si allows for the readout of both the ^{121}Sb and ^{75}As hyperfine state populations and allows for the efficient hyperpolarization of ^{75}As, just as for ^{31}P. These optical polarization and readout techniques were employed to measure the magnetic resonance properties of ^{75}As donors. In particular, we were able to measure long coherence times for all six NMR transitions of ^{75}As donors in ^{28}Si, make them viable candidates for qudits in quantum information processing technologies. These coherence times, however, should only be considered lower bounds, as the coherence times of ^{75}As in a sample with impurity concentrations a few orders of magnitude lower would likely be significantly longer. Since the readout of nuclear spin populations for ^{209}Bi in ^{28}Si using D^0X transitions has already been demonstrated [19], the only remaining question regarding the utilization of D^0X transitions for initializing and reading out the nuclear spins of shallow donor impurities in ^{28}Si is the suitability of resonant pumping of the ^{209}Bi D^0X transitions for achieving nuclear-hyperpolarization. Going beyond ensemble measurements, the use of D^0X resonant Auger photoionization to address specific hyperfine states of specific D^0 in single- or few-donor nanodevices remains a tantalizing but as yet unproven possibility.

ACKNOWLEDGMENTS

This work was supported by the Natural Sciences and Engineering Research Council of Canada (NSERC).

[1] F. A. Zwanenburg, A. S. Dzurak, A. Morello, M. Y. Simmons, L. C. L. Hollenberg, G. Klimeck, S. Rogge, S. N. Coppersmith, and M. A. Eriksson, Rev. Mod. Phys. **85**, 961 (2013).

[2] A. Morello, J. J. Pla, F. A. Zwanenburg, K. W. Chan, K. Y. Tan, H. Huebl, M. Möttönen, C. D. Nugroho, C. Yang, J. A. van Donkelaar *et al.*, Nature (London) **467**, 687 (2010).

[3] J. J. Pla, K. Y. Tan, J. P. Dehollain, W. H. Lim, J. J. Morton, D. N. Jamieson, A. S. Dzurak, and A. Morello, Nature (London) **489**, 541 (2012).

[4] A. M. Tyryshkin, S. Tojo, J. J. Morton, H. Riemann, N. V. Abrosimov, P. Becker, H.-J. Pohl, T. Schenkel, M. L. Thewalt, K. M. Itoh *et al.*, Nat. Mater. **11**, 143 (2012).

[5] J. J. Morton, A. M. Tyryshkin, R. M. Brown, S. Shankar, B. W. Lovett, A. Ardavan, T. Schenkel, E. E. Haller, J. W. Ager, and S. Lyon, Nature (London) **455**, 1085 (2008).

[6] P. Gumann, O. Patange, C. Ramanathan, H. Haas, O. Moussa, M. Thewalt, H. Riemann, N. Abrosimov, P. Becker, H.-J. Pohl *et al.*, Phys. Rev. Lett. **113**, 267604 (2014).

[7] J. T. Muhonen, J. P. Dehollain, A. Laucht, F. E. Hudson, R. Kalra, T. Sekiguchi, K. M. Itoh, D. N. Jamieson, J. C. McCallum, A. S. Dzurak *et al.*, Nat. Nanotechnol. **9**, 986 (2014).

[8] D. Karaiskaj, M. L. W. Thewalt, T. Ruf, M. Cardona, H.-J. Pohl, G. G. Deviatych, P. G. Sennikov, and H. Riemann, Phys. Rev. Lett. **86**, 6010 (2001).

[9] M. Cardona and M. L. W. Thewalt, Rev. Mod. Phys. **77**, 1173 (2005).

[10] A. Yang, M. Steger, D. Karaiskaj, M. L. W. Thewalt, M. Cardona, K. M. Itoh, H. Riemann, N. V. Abrosimov, M. F. Churbanov, A. V. Gusev, A. D. Bulanov, A. K. Kaliteevskii, O. N. Godisov, P. Becker, H.-J. Pohl, J. W. Ager, and E. E. Haller, Phys. Rev. Lett. **97**, 227401 (2006).

[11] A. Yang, M. Steger, T. Sekiguchi, M. L. W. Thewalt, J. W. Ager, and E. E. Haller, Appl. Phys. Lett. **95**, 122113 (2009).

[12] M. Steger, T. Sekiguchi, A. Yang, K. Saeedi, M. E. Hayden, M. L. W. Thewalt, K. M. Itoh, H. Riemann, N. V. Abrosimov, P. Becker, and H. J. Pohl, J. Appl. Phys. **109**, 102411 (2011).

[13] P. Becker, H. J. Pohl, H. Riemann, and N. Abrosimov, Phys. Status Solidi A **207**, 49 (2010).
[14] M. Steger, K. Saeedi, M. L. W. Thewalt, J. J. L. Morton, H. Riemann, N. V. Abrosimov, P. Becker, and H. J. Pohl, Science **336**, 1280 (2012).
[15] K. Saeedi, S. Simmons, J. Z. Salvail, P. Dluhy, H. Riemann, N. V. Abrosimov, P. Becker, H. J. Pohl, J. J. L. Morton, and M. L. W. Thewalt, Science **342**, 830 (2013).
[16] C. Lo, M. Urdampilleta, P. Ross, M. Gonzalez-Zalba, J. Mansir, S. Lyon, M. Thewalt, and J. Morton, Nat. Mater. **14**, 490 (2015).
[17] G. Waldherr, Y. Wang, S. Zaiser, M. Jamali, T. Schulte-Herbrüggen, H. Abe, T. Ohshima, J. Isoya, J. Du, P. Neumann *et al.*, Nature (London) **506**, 204 (2014).
[18] T. Sekiguchi, M. Steger, K. Saeedi, M. L. W. Thewalt, H. Riemann, N. V. Abrosimov, and N. Nötzel, Phys. Rev. Lett. **104**, 137402 (2010).
[19] K. S. Ilkhchy, M. Steger, M. L. W. Thewalt, N. Abrosimov, H. Riemann, P. Becker, and H. J. Pohl, AIP Conf. Proc. **1566**, 552 (2013).
[20] N. J. Stone, At. Data Nucl. Data Tables **90**, 75 (2005).
[21] T. Sekiguchi, A. Tyryshkin, S. Tojo, E. Abe, R. Mori, H. Riemann, N. Abrosimov, P. Becker, H.-J. Pohl, J. Ager *et al.*, Phys. Rev. B **90**, 121203 (2014).
[22] G. Wolfowicz, A. M. Tyryshkin, R. E. George, H. Riemann, N. V. Abrosimov, P. Becker, H.-J. Pohl, M. L. Thewalt, S. A. Lyon, and J. J. Morton, Nat. Nanotech. **8**, 561 (2013).
[23] W. Schmid, Phys. Status Solidi B **84**, 529 (1977).
[24] T. Steiner and M. Thewalt, Solid State Commun. **49**, 1121 (1984).
[25] A. Yang, M. Steger, T. Sekiguchi, M. L. W. Thewalt, T. D. Ladd, K. M. Itoh, H. Riemann, N. V. Abrosimov, P. Becker, and H.-J. Pohl, Phys. Rev. Lett. **102**, 257401 (2009).
[26] S. Simmons, R. M. Brown, H. Riemann, N. V. Abrosimov, P. Becker, H.-J. Pohl, M. L. W. Thewalt, K. M. Itoh, and J. J. L. Morton, Nature (London) **470**, 69 (2011).
[27] W. M. Witzel, R. de Sousa, and S. Das Sarma, Phys. Rev. B **72**, 161306 (2005).